Single-Shot Half *k*-Space High-Resolution Gradient-Recalled EPI for fMRI at 3 Tesla

Andrzej Jesmanowicz, Peter A. Bandettini, James S. Hyde

Half *k*-space gradient-recalled echo-planar imaging (GR-EPI) is discussed in detail. T_2^* decay during full *k*-space GR-EPI gives rise to unequal weighting of the lines of *k*-space, loss of signal intensity at the center of *k*-space, and a point-spread function that limits resolution. In addition, the long readout time for high-resolution full *k*-space acquisition gives rise to severe susceptibility effects. These problems are substantially reduced by acquiring only half of *k*-space and filling the empty side by Hermitian conjugate formation. Details of the pulse sequence and image reconstruction are presented. The point-spread function is $3^{1/2}$ times narrower for half than full *k*-space acquisition. Experiments as well as theoretical considerations were carried out in a context of fMRI using a whole-brain local gradient and an RF coil at 3 Tesla. Using a bandwidth of ±83 kHz, well-resolved single-shot images of the human brain, as well as good quality fMRI data sets were obtained with a matrix of 192 × 192 over 16 × 16 cm² FOV using half *k*-space techniques. The combination of high spatial resolution using the methods presented in this article and the high temporal resolution of EPI opens opportunities for research into fMRI contrast mechanisms. Increase of percent signal change as the resolution increases is attributed to reduction of partial volume effects of activated voxels. Histograms of fMRI pixel responses are progressively weighted to higher percent signal changes as the resolution increases. The conclusion has been reached that half *k*-space GR-EPI is generally superior to full *k*-space GR-EPI and should be used even for low-resolution (64 × 64) EPI.

Key words: echo-planar imaging; functional magnetic resonance imaging; neuroimaging; MRI pulse sequence.

INTRODUCTION

Gradient-recalled echo-planar imaging (GR-EPI) is commonly used for fMRI (1). Full *k*-space trajectories with a 64 × 64 matrix and multislice whole-brain coverage are often used. The matrix can be extended to approximately 96 × 96, and use of interleaving techniques can improve the resolution further (2–4). A 256 × 256 matrix in a 16-shot sequence has been reported (5).

Cohen and Weisskoff (6) have provided a review of the history of EPI. The first EPI articles by Mansfield (7) and Mansfield and Pykett (8) employed partial *k*-space gradient recall on the free induction decay signal, but according to Cohen and Weisskoff (6), the images, although tremendously promising, were not useful. An intense effort to develop EPI methods occurred at the firm of Advanced NMR Systems, Inc., in the period of 1985 to 1990. Most of this effort was directed toward full *k*-space spin-echo EPI (9, 10), although Rzedzian (11) received a patent for a partial *k*-space version. This patent is, to the best of our knowledge, the only formal publication, aside from Mansfield's early articles, that describes partial *k*-space EPI.

Jesmanowicz *et al.* (12) described in an abstract a partial *k*-space gradient-recalled echo-planar sequence and reconstruction at the high spatial resolution of 256 × 256 matrix over 16 × 16 cm² in a single shot over a single slice. The shot-to-shot repetition time for fMRI results presented in the abstract was 1 s. The work was carried out at 3T using a local gradient coil. This article develops that abstract in more detail.

The principles of partial *k*-space trajectories and image reconstruction are well known (see ref. 13). Extension to high-resolution blipped GR-EPI, however, presents several technical complications including a point-spread function that is much greater in the phase-encoding direction than in the frequency-encoding direction, the need for phase and frequency offset correction in the frequency-encoding direction, and the necessity of staying within Food and Drug Administration (FDA) guidelines for field-switching rates.

Our motivation was to achieve improved fMRI spatial resolution together with adequate temporal resolution to follow details of the hemodynamic response. For this application, issues of fMRI contrast also arise. T_2^* decay is likely to be heterogeneous and nonexponential, as discussed by Yablonsky and Haacke (14). Under the assumption of exponential decay, T_2^* in grey matter has been estimated to be 40 ms at 3T (15, 16). It is well known that the greatest sensitivity to the T_2^* changes that are responsible for blood oxygenation level dependent (BOLD) contrast in fMRI occur when TE = T_2^* (see, for example, refs. 16–18). There are two uncertainties in this estimate: nonexponentiality of T_2^*, as mentioned, and the assumption that lines near the center of *k*-space are most responsible for BOLD contrast in image space.

Half *k*-space acquisition lowers the ratio of signal-to-thermal noise by $2^{1/2}$ relative to full *k*-space acquisition neglecting T_2^* decay. However, for fMRI, half *k*-space gradient-recalled EPI can result in a higher rather than lower contrast-to-noise ratio because of a decreased amount of T_2^* decay during readout and the fact that the center of *k*-space is acquired first. The benefits of partial *k*-space acquisition relative to full *k*-space acquisition increase as the field strength increases and T_2^* decreases. In addition, when using single-shot EPI meth-

ods, the noise in fMRI tends to be dominated by physiological fluctuations (see ref. 19 and citations therein). This noise is actually a spatially encoded signal, but little is known about the spatial distribution. As long as the physiological fluctuations dominate the thermal noise and partial volume effects for the fMRI signal as well as physiological noise can be neglected, the effective signal-to-noise ratio would not be affected by resolution. However, the thermal noise will vary as the square root of the pixel area, and at some as yet unknown spatial resolution, a crossover would be expected to occur where thermal noise and physiological fluctuation signal were equal. The crossover would be expected to vary anatomically, be sensitive to the physiology of the microcirculation (20), depend on the fMRI paradigm, differ for full and half *k*-space acquisition, and depend on technical factors that affect signal strength including RF coil, field strength, and slice thickness.

Our motivation for the present work was to develop a methodology that will permit fMRI experiments at higher spatial or temporal resolution. In this article, partial *k*-space gradient-recalled EPI is described in detail in a context of fMRI at high spatial resolution.

METHODS

The *y* Axis Point-Spread Function

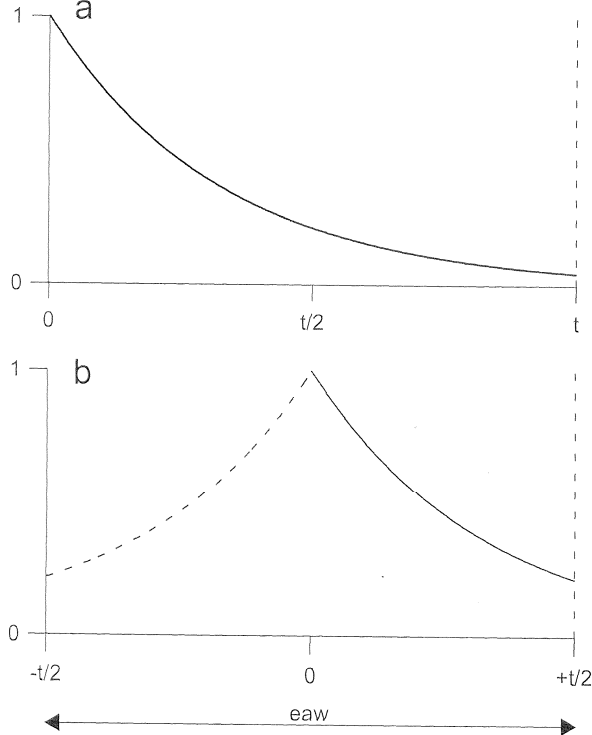Figure 1a illustrates exponential loss of signal intensity

FIG. 1. (a) An example of exponential loss of signal intensity during readout for full *k*-space GR-EPI. Readout is from 0 to *t*. (b) Loss of signal intensity for half *k*-space acquisition using the same exponential as for (a). Readout is from 0 to *t*/2. For negative times (dashed line), the complex conjugates of acquired data are used.

during readout because of T_2^* decay. This is a simulation of conventional full *k*-space GR-EPI for a 128 × 128 matrix ($T_2^* = 40$ ms, bandwidth = ±83 kHz). An initial prephasing gradient centers *k*-space at (eaw)/2 where eaw is the effective acquisition window. One edge of *k*-space corresponding to high spatial frequencies is heavily weighted, whereas the corresponding opposite edge is very weakly weighted and the center of *k*-space is weighted at an intermediate level.

Figure 1b illustrates signal loss for ideal half *k*-space acquisition. The actual readout window begins at $t = 0$ and is of duration (eaw)/2. There is no prephasing gradient in this ideal case. The Hermitian conjugates of these data are used to fill the empty side of *k*-space. This corresponds to negative times in the figure, and the eaw is the same as that of full *k*-space acquisition. In practice, a few so-called overscan lines are required to produce a phase map for reconstruction of the image, and a weak prephasing gradient is required. As is apparent from Fig. 1, the center of *k*-space is optimally weighted for half *k*-space acquisition, and the integrated intensity is greater than for full *k*-space acquisition.

The waveforms of Fig. 1 are given by Eqs. [1] and [2], where H is the Heaviside function. These waveforms give rise to a point spread in image space, as was discussed in refs. 21 and 22 for full *k*-space acquisition. A closed-form expression of the *y* axis point-spread function can be obtained for both waveforms by writing the discrete Fourier transforms, converting them to continuous FTs, and solving the integrals. In both cases, point-spread functions of Lorentzian line shape are obtained when the magnitudes are formed. The half-width at half-height values are given by Eqs. [3] and [4].

$$\alpha(t) = \exp - \left| \frac{t}{T_2^*} \right| \cdot H\left[\frac{t}{T_2^*} \right] \qquad [1]$$

$$\beta(t) = \exp - \left| \frac{t}{T_2^*} \right| \qquad [2]$$

$$\nu_{1/2\alpha} = \frac{\sqrt{3}}{2\pi} \frac{\text{eaw}}{T_2^*} \qquad [3]$$

$$\nu_{1/2\beta} = \frac{1}{2\pi} \frac{\text{eaw}}{T_2^*} \qquad [4]$$

In these equations, the $\nu_{1/2}$ is expressed in units of pixels, which corresponds to a distance in image space. It is notable that the point spread is narrower for half *k*-space acquisition by a factor of $3^{1/2}$ relative to full *k*-space acquisition at the same resolution.

Table 1 lists actual readout times for the experiments described in this paper. Using these values, the point spreads for full and half *k*-space are given in Table 2, assuming $T_2^* = 40$ ms and the image size is 16 × 16 cm². Resolution is limited by pixel size or by the point spread, depending on which is larger. At low resolution, the pixel size dominates, whereas at high resolution the point spread dominates. The entries of Table 2 suggest that 192 × 192 would be a good compromise for the technical parameters used in this work.

Table 1
Echo and Readout Times (ms)

Resolution	TE		Readout time	
	Full k-space	Half k-space	Full k-space	Half k-space
64 × 64	23.0	9.2	37.4	23.6
128 × 128	66.4	12.6	123.8	70.1
192 × 192	134.4	16.1	259.4	141.1
256 × 256	226.9	19.5	444.1	236.7

A simulation comparing half and full k-space acquisition using a one-dimensional phantom has been carried out. Figure 2a illustrates the phantom, with the detailed description given in the figure caption. The phantom of Fig. 2a is convolved with the FT of the $T_2{}^*$ decay waveform to create the one-dimensional images, some of which are shown in Figs. 2b–2e.

Because the effective echo time is longer, the absolute signal intensities for full k-space acquisition are much lower than in half k-space acquisition (Fig. 2). This is because the center of k-space is acquired much later in full than in half k-space acquisition. For example, the signal is too low to display on the same scale for a 256 matrix at full k-space. On the other hand, since the high spatial frequencies for one side of full k-space are acquired first in full k-space acquisition, edges are relatively enhanced in the full k-space cases.

This simulation considers only signal, not noise. At 64 × 64, the signal for full k-space is 65% of the half k-space signal. If thermal noise dominates, the noise in the two halves of k-space will be coherent for partial k-space EPI and incoherent for full k-space EPI, which gives an advantage to full k-space of $2^{1/2}$. The two methods would be virtually identical in SNR when the TE values are in each case as short as practical. If noise is physiological in origin as is the case for fMRI, the noise is spatially encoded, and the simulation of Fig. 2 would reflect the actual SNRs. As the resolution increases, the advantage of half k-space GR-EPI increases rapidly, as is apparent for the 192 × 192 example in Fig. 2.

Scanner

All studies were performed on a 3-T BIOSPEC 30/60 Bruker scanner (Bruker Medizintechnik GMBH, Karlsruhe, Germany). Image reconstruction was done using an HP 748 VME workstation (Hewlett-Packard, Inc., Palo Alto, CA). A balanced torque 3-axis local gradient coil and endcap bandpass birdcage RF coil, as described in refs. 23–25, were used. The rise time was set to 96 μs, a gradient strength of 2.4 G/cm, and a peak field strength of 20 G. The maximum dB/dt was 20 T/s, which is within the 1988 FDA guidelines. The gradient and RF coils were specifically designed for optimum performance over the adult human brain. Use of a local head gradient coil for human EPI studies was introduced by Turner et al. (26).

Use of a local gradient coil with partial k-space EPI permits acquisition of a sufficient number of lines of k-space, as $T_2{}^*$ decay proceeds, to achieve a resolution in the range of 192 × 192 to 256 × 256 over 16 × 16 cm^2

FOV. A trade-off exists between spatial resolution and temporal resolution. In work in progress, partial k-space acquisition using a local gradient coil is being used to extend the temporal resolution at lower spatial resolution (27).

Shim coils of the 60-cm diameter magnet reduce the useful diameter to 53 cm. The gradient coil is at isocenter. It has a nominal diameter of 30 cm and is sufficiently separated from the magnet cryostat walls that gradient eddy currents are minimal. No active gradient shields are employed. The "preemphasis" feature of the Bruker system permits correction of residual eddy-current effects. The gradient rise time in the present study was 96 μs, and the peak gradient strength was 2.4 G/cm. Techron power amplifiers (Model 8607) installed by us provided current to the gradient coil. The FDA dB/dt guideline that is relevant to the present situation is, for axial gradients, that dB/dt $< 2400/\tau$ T/s where τ is the rise time in μs and 12 μs $< \tau < 120$ μs. For transverse gradients, dB/dt should not exceed 3 times the axial limit. In the present experiments for all axial and transverse gradients, dB/dt values were <20 T/s. The gradient coil design in the z direction results in a linear gradient over approximately 18 cm, giving good brain uniformity. The gradient field falls off rapidly at greater distance to stay within FDA guidelines.

A Pentek 16-bit A/D converter with a sampling rate up to 2 MHz was incorporated. An intermediate frequency of 1.25 MHz was employed, with subsampling using an A/D conversion rate of 4/5 of the intermediate frequency, i.e., 1 MHz (28, 29). Odd digitized words provide in-phase information, and even digitized words provide in-quadrature information. Every other odd point (and similarly, every other even point) is inverted in sign, resulting in I (and Q) signal channels. This scheme permits detection of both I and Q in a single amplifier pathway using a single A/D converter. Additional filtering was done digitally, resulting in a bandwidth of ±83 kHz.

Pulse Sequence

The half k-space GR-EPI pulse sequence used here is shown in Fig. 3, and the resulting array of complex data in k-space is shown in Fig. 4a for the case of 256 × 256 matrix dimensions. Eight so-called overscan lines are acquired initially to reach the center of k-space. The central blip is removed, see refs. 30 and 31, to create a redundant pair of lines collected in opposite directions at the center of k-space. These lines are used for horizontal (x axis in k-space) phase and frequency-offset correction. One advantage of the sequence of Fig. 3 is that these two

Table 2
Point Spreads (Half Width at Half Height)

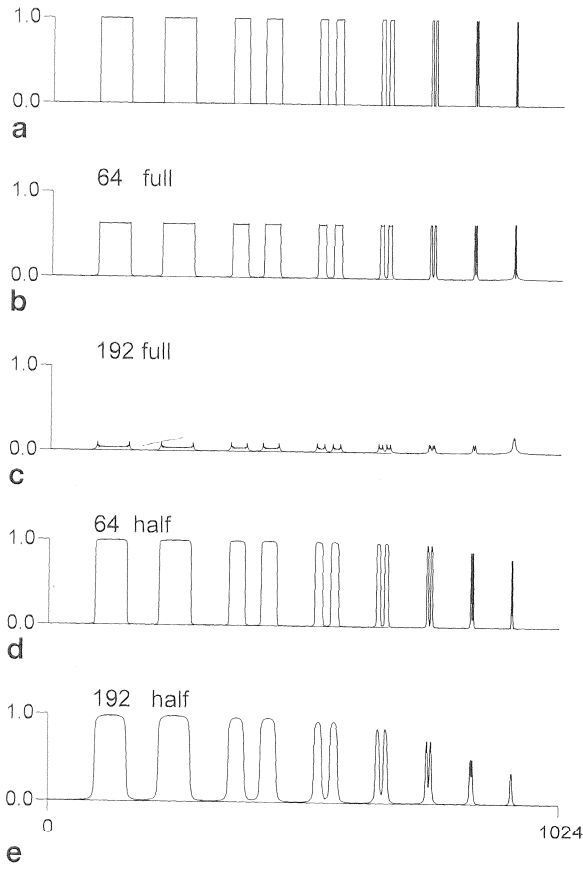| Resolution	Pixel Size (mm)	Full k-space		Half k-space	
		Pixels	mm	Pixels	mm
64 × 64	2.50	0.26	0.65	0.19	0.48
128 × 128	1.25	0.85	1.06	0.56	0.70
192 × 192	0.83	1.79	1.49	1.12	0.93
256 × 256	0.62	3.06	1.91	1.88	1.18

FIG. 2. (a) One-dimensional phantom used for simulations. There are seven pairs of lines. The widths of the lines in each pair are equal and the same as their separation. Widths are in the progression 64, 32, 16, 8, 4, 2, and 1 pixels. (b)–(e) One-dimension simulated images as a function of resolution for full and half k-space acquisitions.

lines are acquired at minimal delay after the 90° pulse and exhibit high SNR. The sequence then proceeds to fill lines 129 to 256 of k-space with 128 readouts. As described later (see Reconstruction section), the eight overscan lines are needed to produce the phase map that is necessary to center the central echo on the central pixel, which is required to fill the empty lines of k-space (region A of Fig. 4a). The area of the prephasing gradient (Fig. 3) equals the total area of the eight y axis overscan blips.

The order of acquisition illustrated in Fig. 3 permits the echo time to be as short as possible, and this is particularly important at higher resolution. Echo times and readout times as a function of spatial resolution are shown in Table 1 for full and half k-space EPI using the scanner parameters given above. As can be seen from Table 1, the echo time for half k-space acquisition is about one-half of T_2^* at 256 × 256 matrix, and the readout time exceeds T_2^* by a factor of 5 or 6. For fMRI, it is estimated that use of a TE of 20 ms with a T_2^* of 40 ms reduces fMRI contrast relative to use of a TE of 40 ms by 15%, which is acceptable. However, a question can be

raised about whether the last lines of k-space acquired in the 256 × 256 half k-space sequence can in principle make a meaningful contribution to resolution when T_2^* is 40 ms. This question is addressed experimentally in the Results section. Since T_2^* is presumably heterogeneous and decay is likely to be nonexponential (14), an experimental approach is appropriate. If full k-space were to be acquired, there would be very little signal intensity remaining at the center, which would be very deleterious. A calculation of fMRI contrast for full k-space 256 × 256 acquisition assuming $T_2^* = 40$ ms and TE = 226.9 ms shows that the contrast drops by a factor of 20 relative to the contrast when TE = 40 ms.

In summary, the central issue in single-shot high-resolution GR-EPI arises in the trade-off between the number of lines of k-space that must be acquired and decay of signal intensity because of T_2^*. Use of partial k-space sequences reduces the number of lines that must be acquired for a given matrix size by approximately a factor of two. This in turn permits the use of a shorter echo time. The reduction in TE for half k-space acquisition becomes increasingly significant as the resolution increases (see Table 1) because the center of k-space progressively drops in intensity for full k-space acquisition.

Reconstruction

Reconstruction issues associated with partial k-space acquisition were summarized by Margosian (32). Purdy (33, 34) proposed a method of reconstruction of half k-space data sets that has been followed with minor modifications in this work.

Figure 4a is a diagram of k-space in which lines of data actually acquired are indicated by the shaded area. In addition to acquisition of half k-space, lines 129–256, N overscan lines are acquired adjacent to line 129. In Fig. 4a and in all of the work described here, N = 8. Acquisition begins with line 121 and proceeds to line 256. As discussed above and illustrated in Table 1, this order of
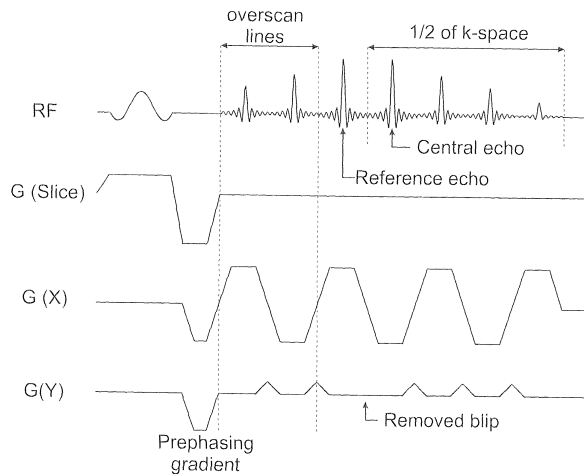

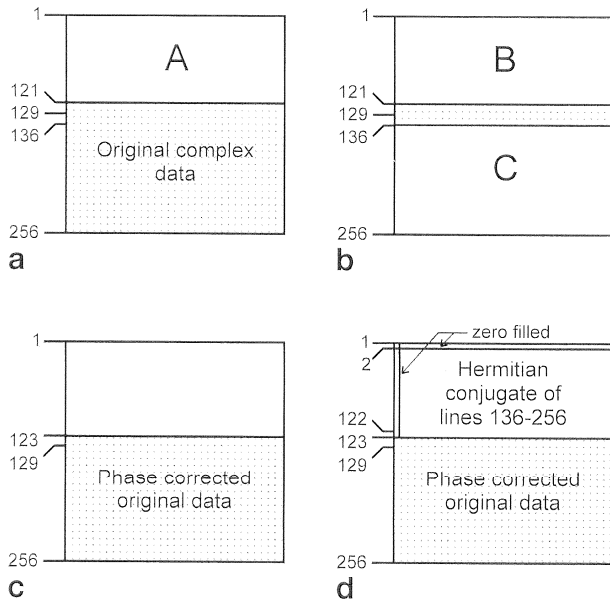FIG. 3. GR-EPI half k-space pulse sequence used in the present work.

FIG. 4. Half k-space reconstruction for the case of 256 × 256. (a) The original data including eight overscan lines. (b) Reduced data set used to produce the phase map. (c) Phase-corrected original data. (d) Filling of k-space by Hermitian conjugate formation.

acquisition results in a much shorter TE value than would be the case if one scanned from line 1 to line 136 or, equivalently, from line 256 to line 121.

According to the symmetries of the FT, if the raw data have a symmetrical real part (I) and an asymmetrical imaginary part (Q), then the image is purely real as, of course, it must be. The first step in reconstruction is to center the data on line 129 of k-space such that I and Q have the requisite symmetries. The reduced I and Q matrices are formed from the lines of k-space shown in Fig. 4b, inserting zeroes in spaces B and C. These data are Fourier-transformed to produce 256 × 256 real and imaginary images. From these images, a pixel-by-pixel phase map (arc tan(I_M/Q_M)), where I_M and Q_M refer to the image real and imaginary intensities, is constructed and saved. This phase map has dimensions of 256 × 256, but actually has 256 resolution only in the x direction. It is smoothed in the y direction as would be expected for 2N resolution.

The original data set (Fig. 4a) is transformed to image space and the phase map is used to correct the values such that all information resides in I_M and no intensity is left in Q_M except for small discrepancies between the actual y axis image resolution and the y axis smoothed phase map. The phase-corrected image is then brought back to k-space by inverse FT (Fig. 4c). The data are now centered on line 129.

With the data centered and phase corrected, the top part of k-space is filled by the Hermitian conjugate of the lower part according to Eq. [5] (see Fig. 4d).

$$\mathrm{raw}(-kx, -ky) = \mathrm{raw}^*(kx, ky) \qquad [5]$$

Note that only lines 2–122 are filled. No data exist to fill line 1, and it is set to zero. It is also necessary to zero-fill one-half of a vertical column, as indicated in Fig. 4d. Original phase-corrected data are used for lines 123–128. Use of six phase-corrected lines for 123–128 and two Hermitian conjugate lines for 121 and 122 was determined empirically and is a trade-off between SNR and artifacts. Finally, the complex data of Fig. 4d are transformed to image space.

The final image is produced by forming $[I_M^2 + Q_M^2]^{1/2}$. In principle, all data should be real, and image I_M should be sufficient. In practice, forming the image from the square root of the sum of the squares suppresses effects of residual phase errors as well as a few pixels with negative values of I_M. Image formation from I_M alone, setting negative values either to zero or to absolute values was also evaluated.

The two-pass phase-correction method suggested by Purdy (33) was implemented in the present work but gave no apparent benefit, presumably because the original EPI data are so low in quality compared with conventional spin warp data. Geometrical error arising from local susceptibility differences between bone, tissue, and air can be corrected using the methods of refs. 35 and 36, but with partial k-space acquisition. A field map is produced by acquiring the last image in the data set using a TE value that is shifted by 1 ms. For half k-space, the image has only 16-pixel resolution in the phase-encoding direction. However, this is sufficient to obtain a 7 × 7 polynomial magnetic field map, which is the same dimensionality used for standard full k-space algorithms (35, 36).

RESULTS

Phantoms

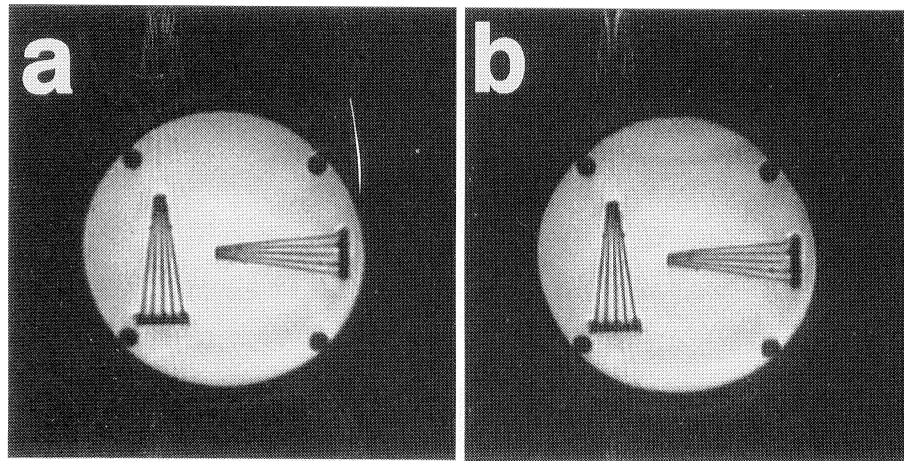A phantom was constructed to evaluate spatial resolution. The T_2 value of the phantom was adjusted by add-

FIG. 5. Single-shot half k-space images. (a) 192 × 192 and (b) 256 × 256 from the resolution phantom. The FOV is 16 × 16 cm² and the phase-encoding direction is vertical.

Wide Plane   Narrow Plane

128^2

192^2

192^2

256^2

256^2

256^2

256^2
truncated

256^2
enhanced

-1.0   -0.5   0.0   0.5   1.0
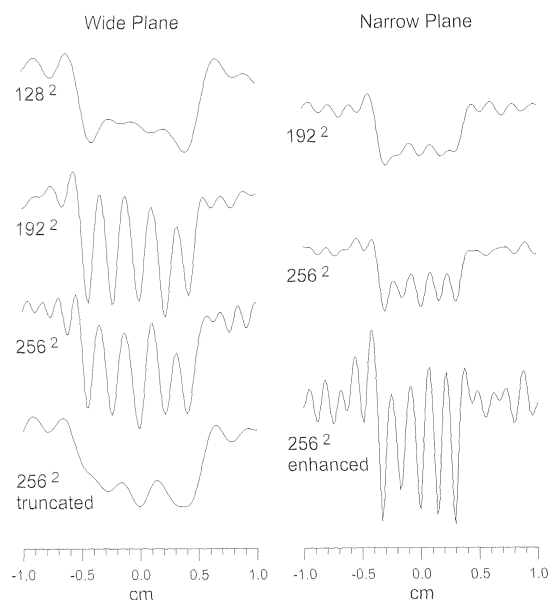cm

-1.0   -0.5   0.0   0.5   1.0
cm

FIG. 6. Resolution profiles. See RESULTS: Phantoms section for details.

ing $CuSO_4$ until it was approximately equal to T_2^* of the brain. A value of 50 ms was measured in the phantom. Figure 5 shows half *k*-space images at (a) 192 × 192 (reconstructed to 256 × 256 by zero filling) and (b) 256 × 256. Figure 6 shows resolution profiles along two vertical lines, one closer to the apex of the object on the right and the other farther from the apex. The more widely spaced struts, when farther from the apex, cannot be resolved at 128 × 128 but can be readily resolved at 192 × 192. The more closely spaced struts at the line closer to the apex cannot be resolved at 192 × 192 but can be resolved at 256 × 256. The point-spread function and lower signal intensity at the outer edge of *k*-space lower the resolution; nevertheless, it is better than if these lines had not been acquired at all.

The profile labeled "256^2 truncated" was obtained by using only the first 64 lines of *k*-space of the data set of the 256^2 profile above to arrive at 256 × 128 and displayed as a 256 × 256 image. It is markedly lower in resolution. This trace establishes the importance of the outer lines of *k*-space in 256^2 image formation even in the presence of substantial T_2^* decay.

The profile labeled "256^2 enhanced" was obtained by artificially eliminating T_2^* decay by multiplying the exponential decay by an exponentially increasing function. The result is increased resolution but with lower SNR. Imaging situations

may exist where this trade-off between resolution and SNR is useful to explore.

Figure 7 shows 256 × 256 single-shot full (a) and half (b) *k*-space images from a three-dimensional grid phantom. The 1.25 × 1.25 × 1.25 cm cubicles are separated by plastic septa. Not only is the full *k*-space image noisier, but also signal dropout because of the long echo time (227 ms) for full *k*-space compared with 20 ms for half *k*-space is much more pronounced (see Table 1). The scalloped appearance of the septa arises from an off-resonance susceptibility effect that depends on the time between readouts of adjacent lines. It is the same for both full and partial *k*-space and can be corrected using field maps (36). Tentatively we attribute small bright spots near dark edges (Fig. 7b) to *y* axis blurring of the phase map.

Human Anatomic Images

Figure 8a shows a 192 × 192 partial *k*-space single-shot image of the human head. Image formation was carried out by zero filling to 256 × 256, followed by the FFT. Figure 8b shows a 256 × 256 partial *k*-space image from the same subject in nearly the same plane-of-section.

These images are very similar, but close inspection reveals some differences. Gibbs artifacts from zero filling of the 192 × 192 data set are more apparent in Fig. 8a. In addition, the image appears somewhat blurred because of the smoothing that occurs from zero filling. Our initial opinion was that Fig. 8b demonstrated higher spatial resolution.

To test this tentative conclusion, the outer 64 lines of the 256 × 256 data set used for Fig. 8b were set to zero, and an image formed that was then subtracted from Fig. 8b. This difference image contained, to a good approximation, only Gibbs artifacts. There appeared to be no additional anatomic information in Fig. 8b compared with Fig. 8a. The reason that Fig. 8b appeared to have better resolution relative to Fig. 8a was not that Fig. 8b exhibited higher resolution through acquisition of outer lines of *k*-space, but rather that Fig. 8a was degraded by Gibbs artifacts arising from zero filling to employ conventional 2D FFT reconstruction in dimensions that are powers of 2.
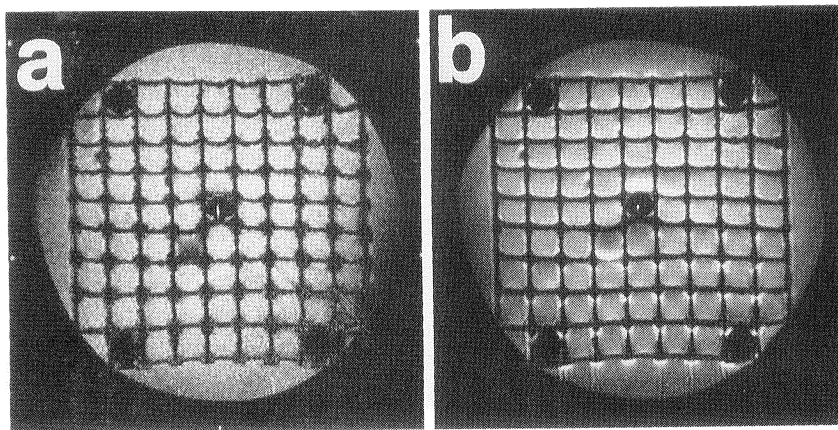
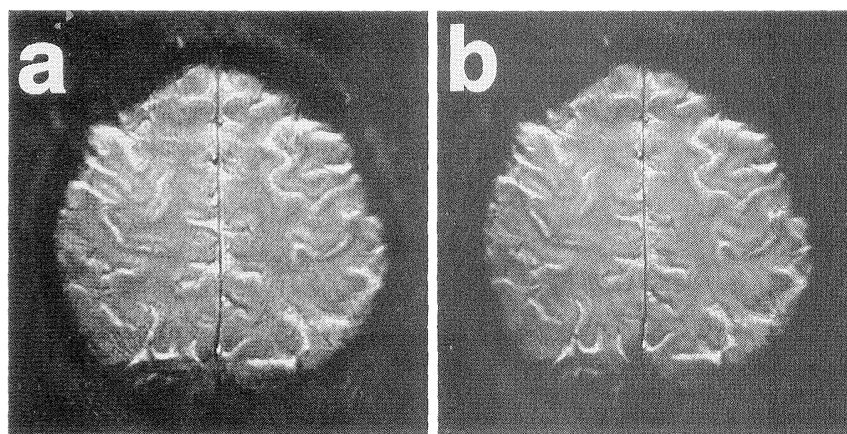FIG. 7. Images from a three-dimensional rectangular grid phantom. (a) Full and (b) half k-space.

FIG. 8. Single-shot GR-EPI anatomic images. (a) 192×192 over 16×16 cm^2, zero filled to 256×256. (b) 256×256.

Within the constraints of FDA dB/dt guidelines, the hardware presently available, and T_2^* in the human head at 3T, 192×192 half k-space acquisition may well be optimum. Reducing the readout time in the x axis for 192×192 relative to 256×256 will improve signal intensity of outer lines of k-space in the phase-encoding (y axis) direction. It is remarked that Gibbs artifacts can be eliminated using a radix FFT procedure that involves powers of 2 plus one power of 3 without significant loss of efficiency (37), noting that $192 = 2^6 \times 3$.

It is concluded that T_2^* decay in the human brain at 3T places a limit on the number of lines of k-space that can be acquired to approximately 96. Partial k-space methods can be used to produce 192×192 images. Improved resolution at 256×256 was seen in the phantom (Fig. 5) where $T_2 = 50$ ms, although the resolution was not improved in the human head where $T_2^* \approx 40$ ms at 3T. The amount of time spent for readout is about eight times greater than the amount of time spent for field switching in the experimental configuration used here. If the gradient strength, the rise time, and the bandwidth were all to be doubled, the resolution would be further improved, and dB/dt would be unchanged. Because T_2^* values are longer at 1.5T (we estimate 60 ms), it is predicted that true 256×256 resolution can be achieved at that field strength using the existing experimental configuration.

fMRI

Half k-space fMRI experiments were carried out to demonstrate feasibility of the sequence for this application. Successive fMRI data sets were obtained one after the other at progressively higher resolutions from 64×64 to 256×256. A conventional finger-tapping paradigm was used. All images were resampled to a resolution of 256×256 for comparison. Magnified correlation images of the right motor cortex region are shown in Figs. 9a, 9b, 9c, and 9d, at progressively higher resolution. See the figure caption for technical details of image acquisition.

Figure 10 is a comparison of histograms of percent enhancement at three different resolutions. A mask in the right motor cortex was created by including any pixel that passed a 0.4 correlation coefficient threshold in at least one of the image sets that were acquired as a function of resolution. Since all images were resampled to 256×256, the number of pixels in the mask was the same for each resolution. The ordinate is the number of
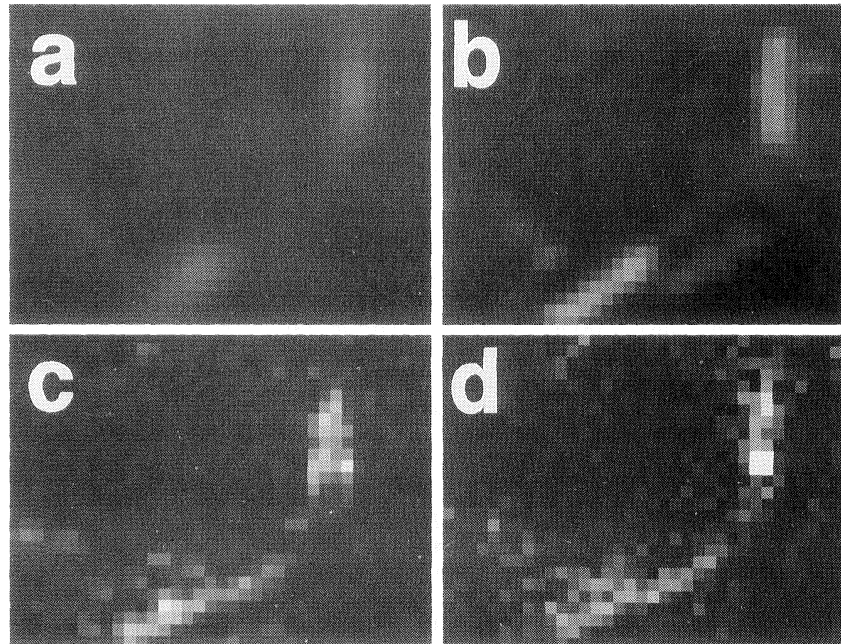

FIG. 9. Percent change maps of the right motor cortex. Slice width was 5 mm, and the FOV was 16 cm. Image matrix sizes and corresponding voxel sizes were: (a) 64×64 and 2.5 mm^2; (b) 128×128 and 1.25 mm^2; (c) 192×192 and 0.83 mm^2; (d) 256×256 and 0.62 mm^2. TE was 20 ms for each image, and the bandwidth was 166.6 kHz. Partial k-space acquisition and conjugate synthesis reconstruction were used for all time series. TR = 1 s. Each time series consisted of 120 images. The bilateral finger-tapping paradigm was 30 s off, 20 s on, 20 s off, 20 s on, 30 s off. All the images were reconstructed onto a 256×256 matrix.
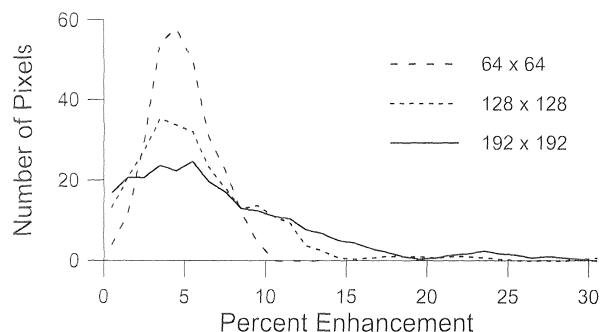
FIG. 10. Histograms of the number of voxels versus percent enhancement as a function of resolution. All voxels in the histograms were obtained from the same region of interest. The data were the same as those used to form the images in Fig. 9.

pixels in a 1% bin. The percent enhancements were determined from the ratio of the signal during finger tapping to the signal at rest for every pixel falling within the mask. A three-point running average was applied to the data to smooth fluctuations. Data for 256×256 are similar to 192×192 and are not plotted in Fig. 10. There are a few pixels that exhibit exceptionally high percent enhancements and are outside the range of the plot of Fig. 10. These include three pixels in the 192×192 image that are above 70% enhancement.

At 64×64 resolution, the percent enhancement is centered at 5%, with very few pixels at 0% to 1% and none above 10%. As the resolution increases, the breadth of the distribution increases progressively. For example, in the range of 10% to 20%, there are no pixels in the 64×64 image, 44 in the 128×128 image, and 62 in the 192×192 image. In the 20% to 30% range, the corresponding numbers are 0, 4, and 11 pixels. Also from Fig. 10, there is a moderate increase in the number of pixels at very low percent enhancement as the resolution increases.

Increase in histogram breadth with increase in resolution is a new result in fMRI. Although other work has shown a decrease in activated area and an increase in percent signal change as resolution increases (16, 38, 39), an increase in the histogram breadth is a clarifying perspective on this result. This comparison of a wide range of EPI resolutions—only possible using half k-space acquisition—clearly demonstrates a reduction in partial volume averaging of inactive regions. The increase in the histogram width toward higher fractional signal changes indicates one or both of the following: (1) An increased stratification of blood volume in each voxel; large vessels are more likely to contribute a large fraction of the signal to a voxel if the voxel is smaller (i.e., closer to the spatial scale of more vessels), whereas the capillary density per voxel is not dependent on resolution (capillary size is much smaller than the voxel scale); (2) decreased partial volume averaging of inactive tissue. The actual units of cortical activation may be on the same scale as the smaller voxels. An increase in the histogram width in the direction of lower fractional signal changes indicates an increase in voxels that do not contribute to the signal changes, which were previously averaged into the lower-resolution signal changes. The slice thickness is relatively large (5 mm) compared with the in-plane voxel dimensions, which suggests that even larger percent enhancements could be obtained by using thinner slices. A general conclusion is that half k-space acquisition offers a new opportunity for investigation of mechanisms of fMRI contrast.

CONCLUSIONS

1. A local gradient coil seems to be required to obtain single-shot high-resolution EPI images within the constraints imposed by the FDA guidelines for field-switching rates. A trade-off exists in local gradient coil design between the gradient rise time and the peak gradient strength. The constraints in determining the trade-off are the point-spread function and the number of lines of k-space that can be acquired with adequate SNR during T_2^* decay. For a given resolution, increased gradient strength and increased bandwidth would increase signal strength because of reduced T_2^* decay, decrease the point spread, and introduce additional thermal noise.

2. Partial k-space acquisition is advantageous for single-shot high-resolution GR-EPI. There are four aspects to this conclusion: First, because of T_2^* decay, the signal intensity is higher. Second, because noise is physiological and spatially encoded, SNR estimates that are based on the assumption of dominant thermal noise are no longer relevant. Third, the point-spread function is narrower in half k-space than in full k-space acquisitions by a factor of $3^{1/2}$. Fourth, loss of signal intensity that arises from dephasing because of bone-tissue-air susceptibility effects is intrinsically reduced in half k-space images because of the reduced TE values.

3. High-resolution, single-shot fMRI data can be achieved at 3T. Images obtained in the present work demonstrate 192×192 resolution over 16 cm^2. A decrease in partial voluming results in substantially increased percent signal change as the resolution increases. In some cases, the first shot in an fMRI time course, which is heavily T_1 weighted, may be adequate as an anatomic image, which would overcome any problems of misregistration arising from susceptibility effects. The condition that TE should equal T_2^* for best contrast-to-noise in fMRI is violated for half k-space acquisition, resulting in a 15% theoretical loss of contrast using TE of 20 ms and assuming T_2^* equals 40 ms. It is much more strongly violated for full k-space acquisition at high resolution, making fMRI essentially impossible (see Table 1).

4. There remain some reconstruction errors in the partial k-space images and there seem to be several opportunities for further improvement of the procedures used here for reconstruction. We have implemented 3/4 k-space acquisition with partial k-space reconstruction. The extra overscan lines improve the phase map and seem to reduce artifacts.

ACKNOWLEDGMENTS

REFERENCES

1. D. Le Bihan, "Diffusion and Perfusion Magnetic Resonance Imaging: Applications to Functional MRI," Raven Press, New York, 1995.

2. G. C. McKinnon, Ultrafast interleaved gradient-echo-planar imaging on a standard scanner. *Magn. Reson. Med.* **30**, 609–616 (1993).

3. K. Butts, S. J. Riederer, R. L. Ehman, J. P. Felmlee, R. C. Grimm, Echo-planar imaging of the liver with a standard MR imaging system. *Radiology* **189**, 259–264 (1993).

4. K. Butts, S. J. Riederer, R. L. Ehman, R. M. Thompson, C. R. Jack, Interleaved echo planar imaging on a standard MRI system. *Magn. Reson. Med.* **31**, 67–72 (1994).

5. S. G. Tan, A. W. Song, E. C. Wong, J. S. Hyde, S.-J. Li, High resolution fMRI with interleaved EPI, *in* "Proc., SMR, 3rd Annual Meeting, Nice, 1995," p. 796.

6. M. S. Cohen, R. M. Weisskoff, Ultra-fast imaging. *Magn. Reson. Imaging* **9**, 1–37 (1991).

7. P. Mansfield, Multi-planar image formation using NMR spin echoes. *J. Phys. C: Solid State Phys.* **10**, L55–L58 (1977).

8. P. Mansfield, I. L. Pykett, Biological and medical imaging by NMR. *J. Magn. Reson.* **29**, 355–373 (1978).

9. I. L. Pykett, R. R. Rzedzian, Instant images of the body by magnetic resonance. *Magn. Reson. Med.* **5**, 563–571 (1987).

10. R. R. Rzedzian, I. L. Pykett, Instant images of the human heart using a new, whole-body MR imaging system. *AJR* **149**, 245–250 (1987).

11. R. R. Rzedzian, Method of high speed imaging with improved spatial resolution using partial k-space acquisitions. U. S. Patent 4,767,991, serial number 085568, issued August 30, 1988.

12. A. Jesmanowicz, P. A. Bandettini, J. S. Hyde, Single-shot half NEX 256 × 256 resolution EPI at 3 Tesla, *in* "Proc., ISMRM, 5th Annual Meeting, Vancouver, 1997," p. 1632.

13. G. McGibney, M. R. Smith, S. T. Nichols, A. Crawley, Quantitative evaluation of several partial Fourier reconstruction algorithms used in MRI. *Magn. Reson. Med.* **30**, 51–59 (1993).

14. D. Yablonsky, E. M. Haacke, Theory of NMR signal behavior in magnetically inhomogeneous tissues: the static dephasing regime. *Magn. Reson. Med.* **32**, 749–763 (1994).

15. P. A. Bandettini, E. C. Wong, A. Jesmanowicz, R. Prost, R. W. Cox, R. S. Hinks, J. S. Hyde, MRI of human brain activation at 0.5 T, 1.5 T, and 3.0 T: comparisons of $\Delta R2^*$ and functional contrast to noise ratio, *in* "Proc., SMRM, 2nd Annual Meeting, San Francisco, 1994," p. 434.

16. P. A. Bandettini, Ph.D. Dissertation, "Magnetic Resonance Imaging of Human Brain Activation using Endogenous Susceptibility Contrast." Medical College of Wisconsin, Milwaukee, 1995.

17. R. S. Menon, S. Ogawa, D. W. Tank, K. Ugurbil, 4 Tesla gradient recalled echo characteristics of photic stimulation-induced signal changes in the human primary visual cortex. *Magn. Reson. Med.* **30**, 380–386 (1993).

18. P. A. Bandettini, E. C. Wong, A. Jesmanowicz, R. S. Hinks, J. S. Hyde, Spin-echo and gradient-echo EPI of human brain activation using BOLD contrast: a comparative study at 1.5 T. *NMR Biomed.* **7**, 12–20 (1994).

19. B. Biswal, F. Z. Yetkin, V. M. Haughton, J. S. Hyde, Functional connectivity in the motor cortex of resting human brain using echo-planar MRI. *Magn. Reson. Med.* **34**, 537–541 (1995).

20. J. E. W. Mayhew, S. Askew, Y. Zheng, J. Porrill, G. W. M. Westby, P. Redgrave, D. M. Rector, R. M. Harper, Cerebral vasomotion: A 0.1-Hz oscillation in reflected light imaging of neural activity. *Neuroimage* **4**, 183–193 (1996).

21. F. Farzaneh, S. J. Riederer, N. J. Pelc, Analysis of T2 limitations and off-resonance effects on spatial resolution and artifacts in echo-planar imaging. *Magn. Reson. Med.* **14**, 123–139 (1990).

22. G. Johnson, J. M. S. Hutchison, The limitations of NMR recalled-echo imaging techniques. *J. Magn. Reson.* **63**, 14–30 (1985).

23. E. C. Wong, P. A. Bandettini, J. S. Hyde, Echo-planar imaging of the human brain using a three axis local gradient coil, *in* "Proc., SMRM, 11th Annual Meeting, Berlin, 1992," p. 105.

24. E. C. Wong, E. Boskamp, J. S. Hyde, A volume optimized quadrature elliptical endcap birdcage brain coil, *in* "Proc., SMRM, 11th Annual Meeting, Berlin, 1992," p. 4015.

25. E. C. Wong, G. Tan, J. S. Hyde, A quadrature transmit-receive endcapped birdcage coil for imaging of the human head at 125 MHz, *in* "Proc., SMRM, 12th Annual Meeting, New York, 1993," p. 1344.

26. R. Turner, R. Vavrek, J. Maier, D. Le Bihan, EPI diffusion imaging of the brain at 1.5 Tesla without motion artifact using a localized head gradient coil, *in* "Proc., SMRM, 8th Annual Meeting, Amsterdam, 1989, p. 1123.

27. B. Biswal, A. Jesmanowicz, J. S. Hyde, High temporal resolution FMRI, *in* "Proc., ISMRM, 5th Scientific Meeting, Vancouver, 1997," p. 1629.

28. R. S. Stormont, M. C. Anas, N. J. Pelc, Radio frequency receiver for a NMR instrument. US Patent 4,992,736, serial number 309456, issued February 12, 1991.

29. R. S. Stormont, J. P. Noon, N. J. Pelc, N. R. Hattes, M. D. Anas, R. H. Horwarth, R. Glusick, A new transceiver for MR imaging and spectroscopy. *in* "SMR Book of Abstracts, Volume 1, 8th Annual Meeting, Amsterdam, 1989," p. 962.

30. A. Jesmanowicz, E. C. Wong, J. S. Hyde, Phase correction for EPI using internal reference lines, *in* "Proc., SMRM, 12th Annual Meeting, New York, 1993," p. 1239.

31. A. Jesmanowicz, E. C. Wong, J. S. Hyde, Self-correcting EPI reconstruction algorithm, *in* "Proc., SMR, 3rd Annual Meeting, Nice, 1995," p. 619.

32. P. Margosian, Faster MR imaging: imaging with half the data, *in* "Proc., SMRM, 4th Annual Meeting, London, 1985," pp. 1024–1025.

33. D. E. Purdy, A double phase correction/Hermitian conjnjugate procedure improves the quality of half-Fourier images, *in* "Proc., SMRM, 6th Annual Meeting, New York, 1987," p. 379.

34. D. E. Purdy, A Fourier transform method of obtaining high resolution phase maps for half-Fourier imaging, *in* "Proc., SMRM, 7th Annual Meeting, San Francisco, 1988," p. 968.

35. A. Jesmanowicz, J. S. Hyde, Single-pass automatic 3D shimming, *in* "Proc., ISMRM, 5th Scientific Meeting, Vancouver, 1997," p. 1983.

36. A. Jesmanowicz, J. S. Hyde, Real-time two-shot EPI auto shim overall shimming polynomials, *in* "Proc., SMR, 3rd Annual Meeting, Nice, 1995," p. 618.

37. C. Lu, J. W. Cooley, R. Tolimieri, FFT algorithms for prime transform sizes and their implementations of VAX, IBM 3090VF, and IBM RS/6000. *IEEE Trans. Acoust. Speech Signal Proc.* **41**, 638–648 (1993).

38. S. Lai, A. L. Hopkins, E. M. Haacke, D. Li, B. A. Wasserman, P. Buckley, L. Friedman, H. Meltzer, P. Hedera, R. Friedland, Identification of vascular structures as a major source of signal contrast in high resolution 2D and 3D functional activation imaging of the motor cortex at 1.5T: preliminary results. *Magn. Reson. Med.* **30**, 387–392 (1993).

39. J. Frahm, K.-D. Merboldt, W. Hänicke, Functional MRI of human brain activation at high spatial resolution. *Magn. Reson. Med.* **29**, 139–144 (1993).